Journal of Solid State Chemistry 287 (2020) 121380

(DOI: 10.1016/j.jssc.2020.121380)

https://doi.org/10.1016/j.jssc.2020.121380

Thermoanalytical, optical, and magnetic investigations on nanocrystalline $Li_{0.5}Fe_{2.5}O_4$ and resulting ceramics prepared by a starch-based soft-chemistry synthesis

Roberto Köferstein

Institute of Chemistry, Martin Luther University Halle-Wittenberg,

Kurt-Mothes-Straße 2, 06120 Halle, Germany.

Dedicated to Professor Christian Robl on the occasion of his 65th birthday

Tel.: +49-345-5525630; Fax: +49-345-5527028.

E-mail address: roberto.koeferstein@chemie.uni-halle.de

Abstract. Nanocrystalline $Li_{0.5}Fe_{2.5}O_4$ was prepared by a starch-based soft-chemistry synthesis. Calcining of the (LiFe)-gel between 350 and 1000 °C results in $Li_{0.5}Fe_{2.5}O_4$ powders with crystallite sizes from 13 to 141 nm and specific surface areas between 35 and 7.1 m^2 g^{-1}. XRD investigations reveal the formation of ordered $Li_{0.5}Fe_{2.5}O_4$. Sintering between 1050 and 1250 °C leads to ceramics with relative densities of 67–95 % consisting of grains between 0.3 and 54 µm. As the sintering temperature increases a rising weight loss of the ceramic samples was observed due to the loss of Li_2O. Temperature-dependent magnetic measurements indicate a superparamagnetic behaviour for the nano-sized samples. Field-dependent measurements at 3 K of ceramics sintered between 1050 and 1200 °C show increasing saturation magnetization values (M_s) of 70.0 to 73.0 emu g^{-1} most likely due to the formation of lithium vacancies and a decrease of the inversion parameter. The magnetization drops down to 67.7 emu g^{-1} after sintering at 1250 °C caused by the formation of hematite. Diffuse reflectance spectra reveal an indirect allowed band gap decreasing from 1.93 to 1.60 eV depending on thermal treatment. DSC measurements of the order ⇆ disorder phase transition on nano-sized powders and bulk ceramics exhibit transition temperatures between

734 and 755 °C and enthalpy changes ($\Delta_{trs}H$) ranging from 5.0 to 13.5 J g^{-1}. The linear thermal expansion coefficient was found to be $11.4 \cdot 10^{-6}$ K^{-1}.

Keywords: *spinel; nano-particle; band-gap, magnetism, phase transition*

1. Introduction

$Li_{0.5}Fe_{2.5}O_4$ ($LiFe_5O_8$) has interesting technological applications such as microwave, optical isolator, and memory devices because of its high saturation magnetization and Curie temperature [1,2,3]. Lithium ferrite can be also used as electrode material in lithium ion batteries [4,5]. In addition, $Li_{0.5}Fe_{2.5}O_4$ act as catalyst for the synthesis of biodiesel and β-amino ketones as well as photocatalyst for the decomposition of organic compounds and for water splitting [6–9]. Furthermore, Rezlescu et al. [10] reported on lithium ferrite for gas sensing applications. Moreover, a magnetoelectric effect was found in $Li_{0.5}Fe_{2.5}O_4$ as well as in $BaTiO_3$–$Li_{0.5}Fe_{2.5}O_4$ composites [11,12].

$Li_{0.5}Fe_{2.5}O_4$ crystallizes in the inverse spinel structure and occurs in an ordered form (α-form, SG: $P4_332$) and a disordered one (β-form, SG: $Fd\bar{3}m$) [13]. The reversible ordered ⇆ disordered phase transition in bulk material take place at about 750 °C and a Curie temperature of about 630 °C was found [14]. The disordered form (β-$Li_{0.5}Fe_{2.5}O_4$) can be obtained by rapid quenching of samples from high temperatures to room temperature, whereas the ordered spinel phase forms upon slow cooling. At high temperatures, $Li_{0.5}Fe_{2.5}O_4$ loses lithium and oxygen which influences the magnetic and electrical properties [15,16].

Polycrystalline $Li_{0.5}Fe_{2.5}O_4$ samples are commonly synthesized by the conventional mixed-oxide method which requires high calcining temperatures leading to large particles and high sintering temperatures [17]. Whereas, soft-chemistry syntheses require low reaction temperatures to synthesize nano-sized samples. Various soft-chemical syntheses have been reported, such as hydrothermal [18], solvothermal [19], sol-gel [20,21], combustion [22,23] and precursor routes [24]. Closer inspection shows, that various synthesis routes lead to $Li_{0.5}Fe_{2.5}O_4$ with traces of hematite [25–28]. In order to avoid the formation of iron-rich secondary phases an excess of lithium was used [29–31]. The formation of β-$Li_{0.5}Fe_{2.5}O_4$ at low temperatures was reported for some soft-chemical syntheses [18,32,33].

The aim of this paper is to describe a facile synthesis route using starch to prepare nanocrystalline $Li_{0.5}Fe_{2.5}O_4$ powders and ceramic bodies obtained from these powders. Phase evolution during calcination and sintering were monitored by XRD. Furthermore, magnetic measurements between 3 and 300 K were carried out both on calcined powders and ceramic

bodies. Moreover, we determined the order ⇆ disorder phase transition temperature and enthalpy change depending on particle size as well as the linear thermal expansion coefficient of $Li_{0.5}Fe_{2.5}O_4$.

2. Experimental

2.1. Material preparation

$Fe(NO_3)_3 \cdot 9H_2O$ (0.024 mol, Alfa Aesar, ACS reagent), Li_2CO_3 (0.0024 mol, UCB Belgium, ≥ 99 %) and NH_4NO_3 (0.036 mol, Fluka < 99 %) were dissolved in 10 ml deionized water. After addition of 0.0123 mol soluble starch (M = 342.30 g mol^{-1}, Sigma-Aldrich, ACS reagent) the turbid solution was stirred at room temperature until it turned to a highly viscous red gel. This (LiFe)-gel was calcined for 2 h in static air at various temperatures (heating-/cooling rate 5 K min^{-1}) leading to $Li_{0.5}Fe_{2.5}O_4$ nano powders. To obtain ceramic bodies, the (LiFe)-gel was calcined at 350 °C for 2 h. Then, the resulting powder was mixed with 10 wt% of a saturated aqueous polyvinyl alcohol (PVA) solution as a pressing aid and uniaxially pressed at about 85 MPa into pellets (green density 1.5 g cm^{-3}). These pellets were placed on a ZrO_2 fibre mat and sintered to ceramic bodies.

2.2. Characterization

X-ray powder diffraction patterns were recorded at room temperature on a *Bruker D8-Advance* diffractometer, equipped with a one-dimensional silicon strip detector (LynxEye™) using Cu-K_α radiation and a counting time of 1 s per data point. Crystallite size and the strain parameter were calculated from XRD line broadening (integral peak breadth) using the Scherrer and Wilson equations (software suite WinXPOW [34]). Dilatometric measurements were carried out in flowing synthetic air (50 ml min^{-1}) with a rate of 5 K min^{-1} and a contact force of 0.2 N in a *Netzsch* TMA 402F3 dilatometer. Simultaneous thermogravimetric (TG) and differential thermoanalytic (DSC) investigations in flowing synthetic air (50 ml min^{-1}) were performed using a *Netzsch* STA 449F5 system. To study the phase transitions in $Li_{0.5}Fe_{2.5}O_4$, the ceramic bodies were crushed to powders and the DSC curves were performed with a rate of 20 K min^{-1}. The specific surface area (BET) was determined using nitrogen five-point gasphysisorption (Nova touch 2LX, Quantachrome Corporation). The equivalent BET particle diameter was calculated assuming a spherical or cubic particle shape. Scanning electron microscope images were recorded with a *Phenom* ProX SEM in the backscattered electron mode (BSE). Diffuse reflectance spectra were recorded at room temperature using a *Perkin Elmer* UV−Vis spectrometer Lambda 19 with $BaSO_4$ as white standard. Magnetic

measurements were carried out using a Quantum Design PPMS9. Hysteresis loops were taken with magnetic field cycling between –90 and + 90 kOe. In addition, the temperature dependent magnetizations were measured between 3–300 K using field-cooled (FC) and zero-field cooled (ZFC) conditions. The samples were enclosed in gel capsules whose very small contribution to the measured magnetic moment was subtracted before data evaluation.

3. Results and discussion

3.1. Synthesis and powder characterization

The formation of $Li_{0.5}Fe_{2.5}O_4$ was examined by thermal decomposition of the (LiFe)-gel in a muffle furnace in static air (heating rate 5 K min^{-1}, soaking time 2 h). The prepared red (LiFe)-gel is X-ray amorphous (Fig. S1, supporting information). Heating the gel at 300 °C leads to a brown powder. The XRD pattern (Graph 1a) only shows reflections which can be assigned to $Li_{0.5}Fe_{2.5}O_4$. Measurements with a prolonged counting time (see insets in Fig. 1) show the formation of the (210) and (211) superstructure reflections proofing the formation of the ordered $Li_{0.5}Fe_{2.5}O_4$ phase (JCPDS #01-082-1436). Thermoanalytic measurements of the sample calcined at 300 °C show a strong exothermic weight loss of about 17 % up to 800 °C suggesting the presence of undecomposed amorphous compounds. Calcining at 350 °C results in a full decomposition and the formation of ordered lithium ferrite with a light-brown colour (Graph 1b). At 600 °C the superstructure reflections of the ordered phase can be even more clearly seen (Graph 1d). Up to a calcination temperature of 1000 °C no secondary phases appear (Graph 1e). The crystallite size of the calcined $Li_{0.5}Fe_{2.5}O_4$ powders increases from 13(1) nm after thermal treatment at 350 °C to 20(2) nm at 600 °C and to 142(11) nm at 1000 °C (Fig. 2). Likewise, the specific surface area decreases from 35(3) to 7.1(6) m^2 g^{-1} with rising calcining temperature as shown in right scale of Fig. 2.

The presented synthesis led to a significant reduction of the reaction temperature to 350 °C for phase pure ordered $Li_{0.5}Fe_{2.5}O_4$ with a stoichiometric initial Li/Fe ratio of 0.2, compared to the conventional mixed-oxide method and to other wet-chemical syntheses [11,25–27]. The low intensity of the superstructure reflections up to 600 °C is caused by the low degree of order of lithium and iron ions at octahedral sites.

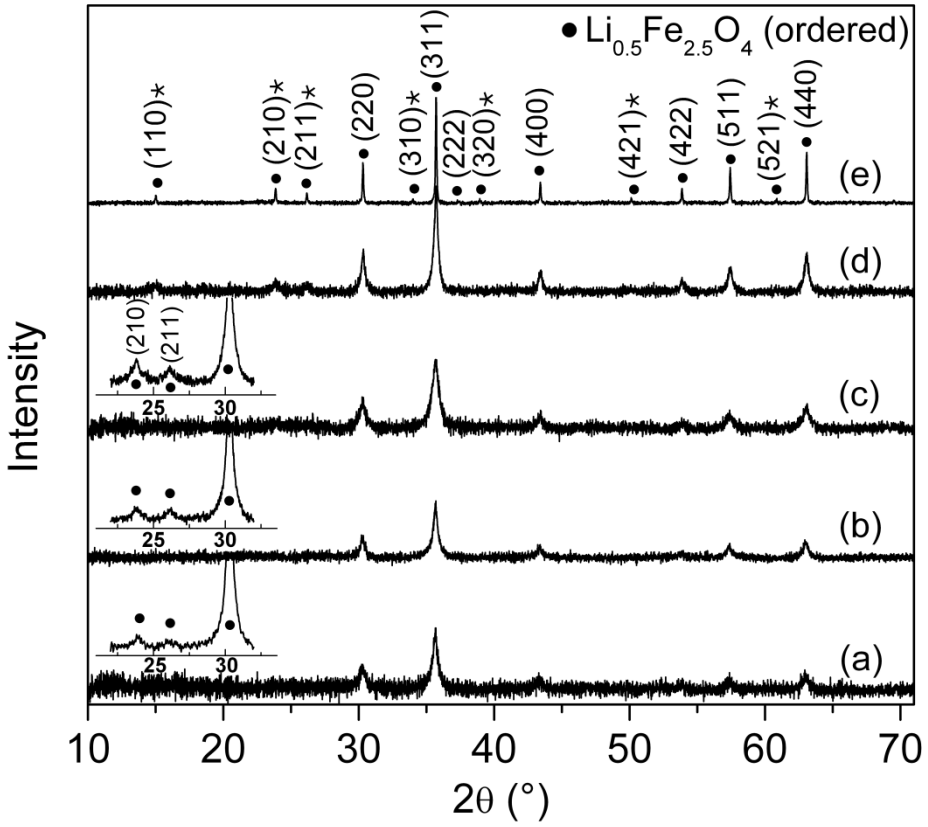

Fig. 1. Room-temperature XRD patterns of the (LiFe)-gel after calcination for 2 h at different temperatures (heating rate 5 K/min): a) 300 °C, b) 350 °C, c) 500 °C, d) 600 °C, and e) 1000 °C. The insets show a magnification of XRD patterns recorded with a prolonged counting time of 10 s and 40 s per data point, respectively. The reflections marked by an asterisk are superstructure reflections.

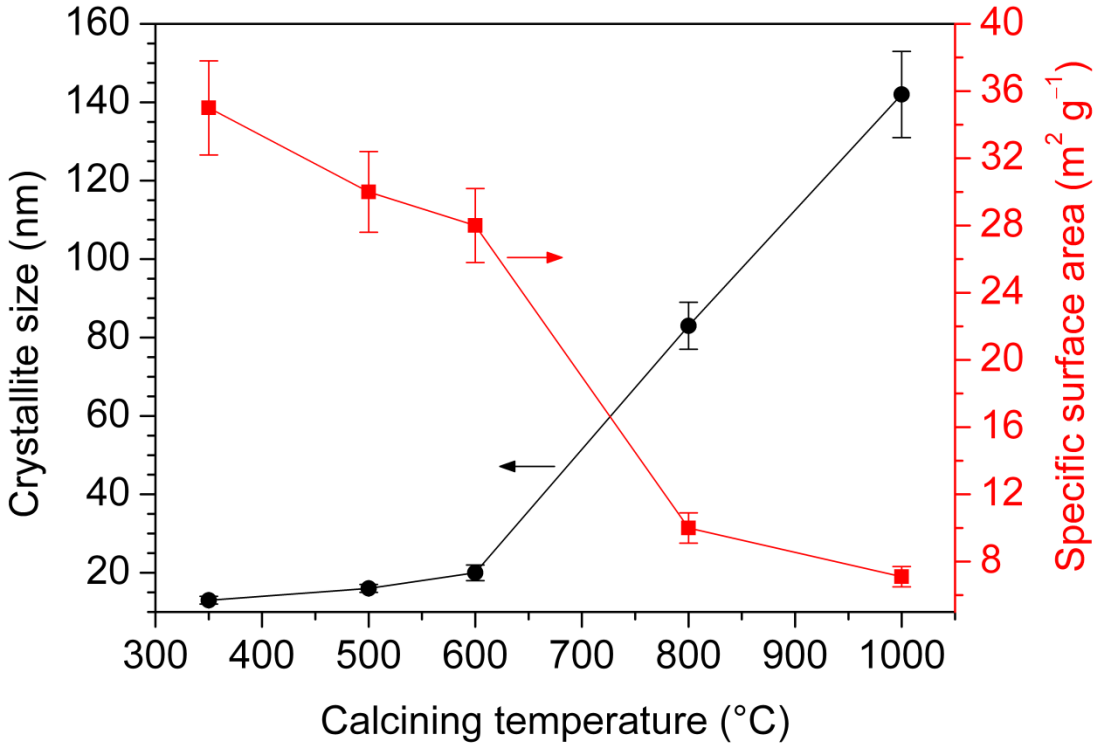

Fig. 2. Evolution of the crystallite size with the calcining temperature. The right scale shows the development of the specific surface area.

3.2. Sintering behaviour and microstructure of ceramic bodies

Prior to investigation of the sintering behaviour, the (LiFe)-gel was calcined at 350 °C for 2 h. As mentioned above, this calcination process leads to a light-brown nanocrystalline $Li_{0.5}Fe_{2.5}O_4$ powder with a volume-weighted average crystallite size of 13(1) nm. The specific surface area of that powder was determined as 35(3) $m^2\ g^{-1}$ corresponding to a calculated equivalent particle size of 36(3) nm. The difference between the crystallite size and the particle size from BET data can be explained by an agglomeration leading to surface areas unavailable for nitrogen adsorption.

This nanocrystalline powder was pressed to pellets and isothermal sintered for 1 h in static air at different temperatures (heating-/ cooling rate: 5 K min^{-1}). The final bulk densities (Fig. 3) of the black-brown ceramic bodies were calculated from their weight and geometric dimensions and related to the single crystal density of 4.72 g cm^{-3} [13]. Sintering at 1000 and 1050 °C results in a poor densification with relative densities of 67(1) and 79(1) %, respectively. Firing at 1100 °C leads to bodies with 90(1) % relative density which increases to 93(1) and 95(1) % at 1150 and 1250 °C, respectively. SEM images of ceramics bodies are shown in Fig. 4. Ceramics sintered at 1050 °C and 1100 °C show irregular grains with a

bimodal type grain size distribution between 0.3–6.5 µm and 0.5–20 µm, respectively (Fig. 4a,b). After firing at 1150 °C the grain sizes range between 1.5 and 36 µm and the average grain size is 6.6(5) µm as determined by the lineal intercept method [35]. The grains grow to 2.5–45 µm ($\varnothing_{li}$ = 11(1) µm) and 2.5–54 µm ($\varnothing_{li}$ = 13(1) µm) at 1200 and 1250 °C, respectively (Fig. 4c,d).

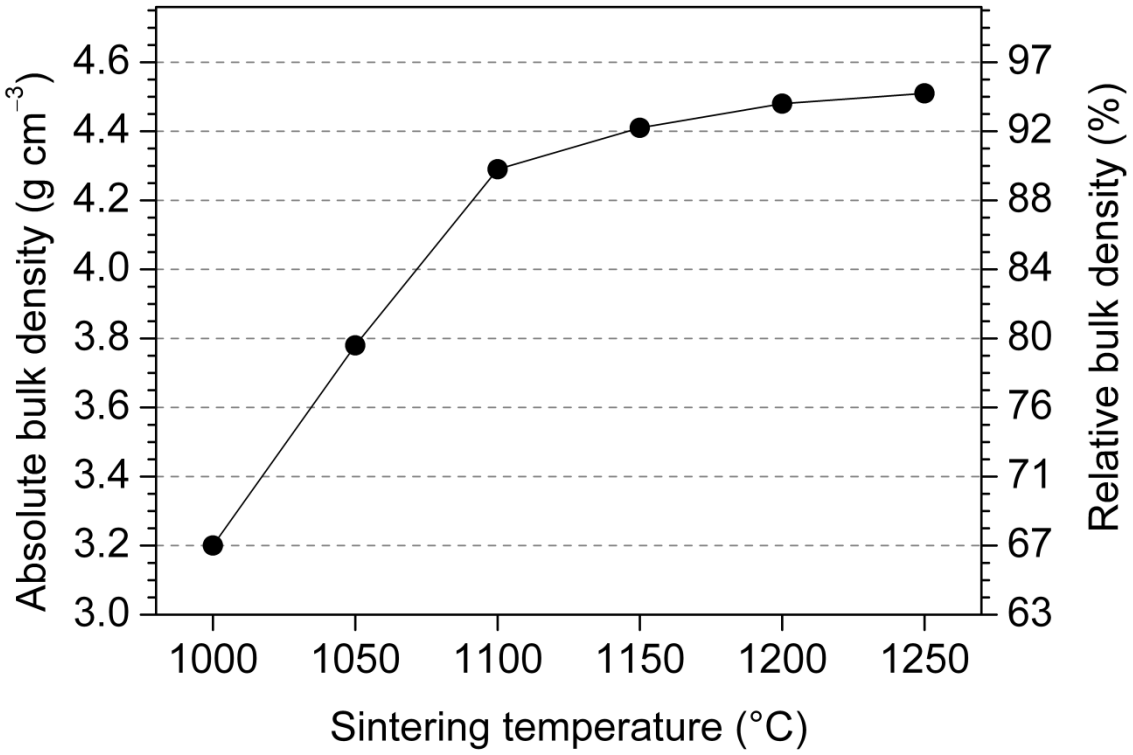

Fig. 3. Bulk densities of ceramic bodies after sintering at various temperatures (soaking time 1 h, heating rate 5 K min^{-1}). Error bars correspond to the size of the symbols.

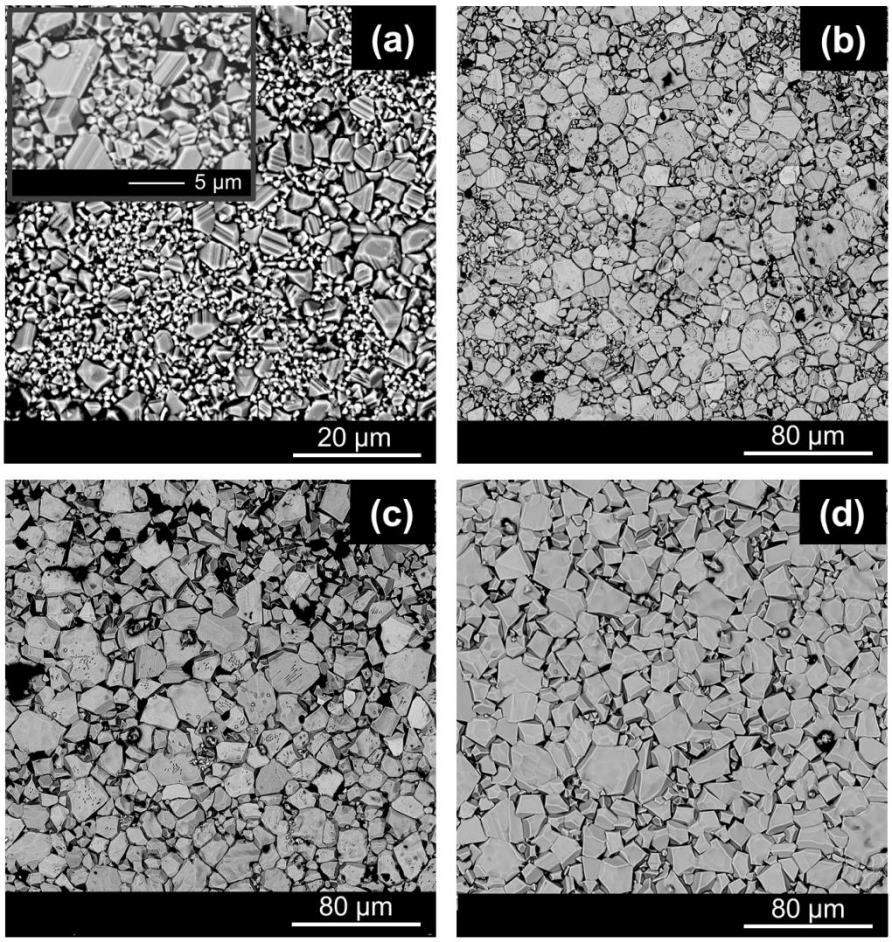

Fig. 4. SEM-BSE images of ceramic bodies sintered for 1 h at (a) 1100 °C, (b)1150 °C, (c) 1200 °C, and (d) 1250 °C.

As reported elsewhere, heating of $Li_{0.5}Fe_{2.5}O_4$ leads to a sublimation of Li_2O [36,37]. To estimate the weight loss during thermal treatment, several powder compacts were fast preheated to 800 °C to burn out the organic binder (PVA) and thermogravimetric measurements were carried out on these compacts. Fig. 5 shows a non-isothermal thermogravimetric measurement in flowing air up to 1250 °C (rate 5 K min^{-1}). A very slight weight loss starts at 750 °C, whereas a strong increase of the weight loss rate was observed above about 1130 °C. After one hour sintering at 1050, 1100, 1150, 1200, 1250 °C, the lithium loss was calculated as 4, 6, 8, 12, and 15 mol% assuming the total weight loss is caused by the loss of Li_2O (inset in Fig. 5). A possible partial reduction of Fe^{3+} to Fe^{2+} was neglected because sintering was carried out in air with low cooling and heating rates [36,37].

XRD patterns of ceramic bodies sintered between 1050 and 1250 °C are shown in Fig. 6. To detect small amounts of secondary phases, the XRD patterns were recorded with a prolonged counting time of 10 s per data point. After one hour sintering up to 1200 °C the XRD patterns do not show any indications of secondary phases, i.e. only reflections of ordered $Li_{0.5}Fe_{2.5}O_4$

can be seen. On the other hand, firing at 1250 °C leads to the formation of very small amounts of Fe_2O_3 (hematite, JCPDS #01-073-2234).

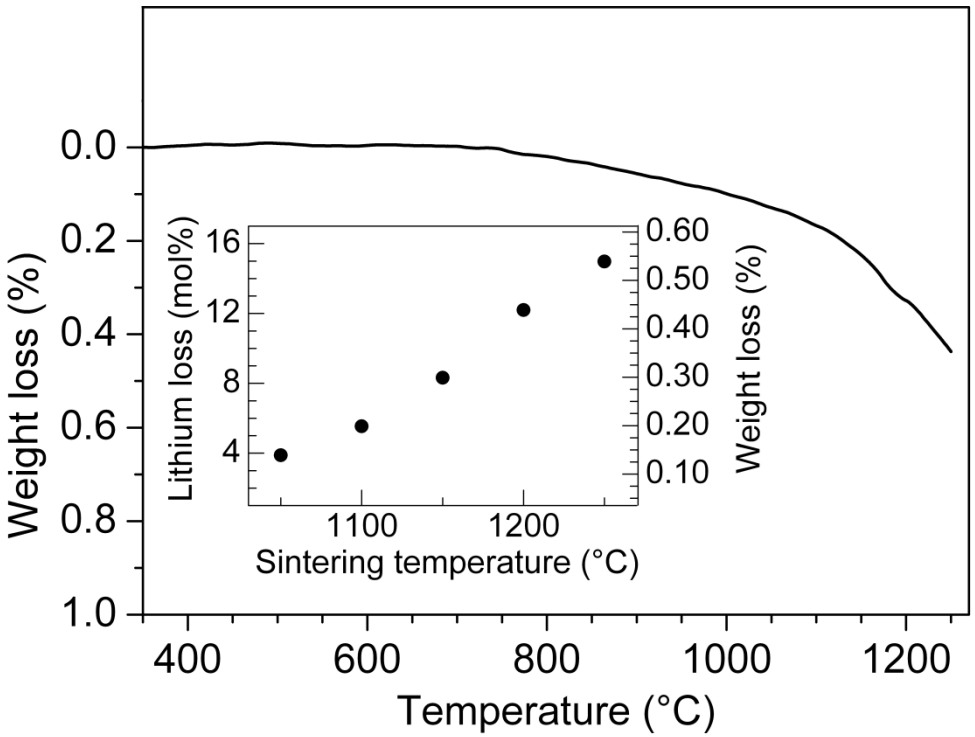

Fig. 5. Thermogravimetric measurement (rate 5 K min^{-1}) of a $Li_{0.5}Fe_{2.5}O_4$ compact in flowing air. The inset shows the total weight loss and the calculated lithium loss after 1 h sintering.

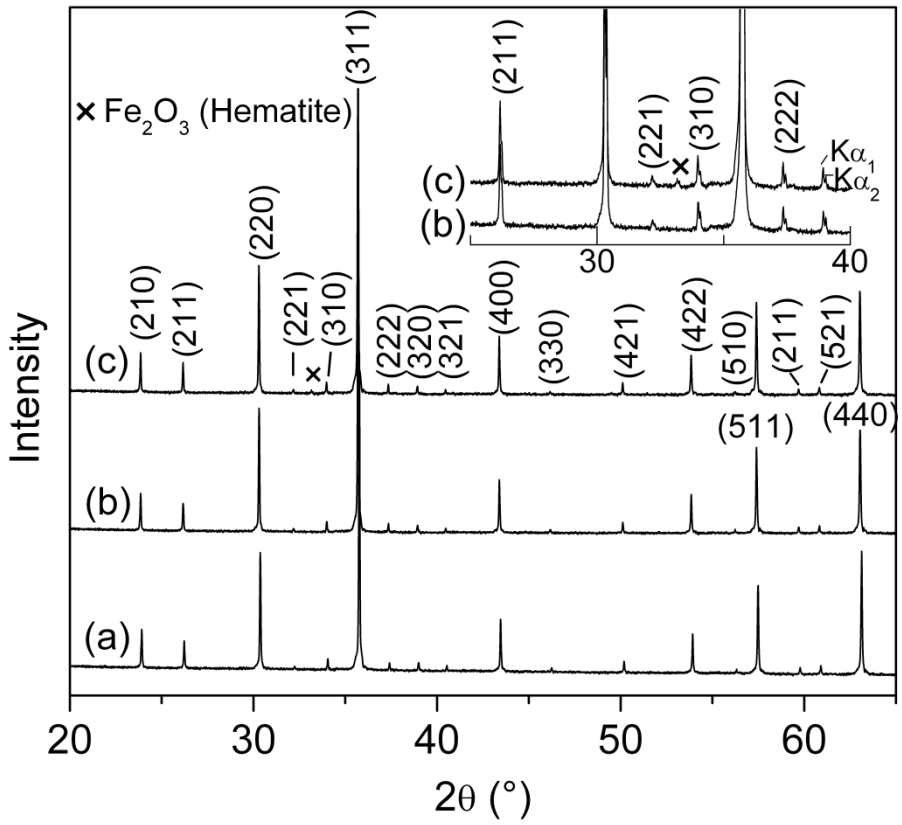

Fig. 6. Room temperature XRD patterns of powdered $Li_{0.5}Fe_{2.5}O_4$ ceramics fired for 1 h at (a) 1050 °C, (b) 1200 °C, and (c) 1250 °C. The patterns were recorded with a counting time of 10 s per data point. The inset shows magnifications of graphs (a) and (c) including the $K\alpha_2$ reflections.

3.3 Magnetic, thermoanalytic, and optical investigations

Fig. 7 shows the temperature-dependent magnetization under ZFC and FC conditions with an applied field (H_{DC}) of 1 kOe for powders calcined between 350 and 800 °C. Up to a calcining temperature of 600 °C the FC curve decreases with rising temperature while the ZFC curve increases up to a maximum. Above this maximum, the so-called blocking temperature (T_B), the ZFC curve decreases. The blocking temperature increases with the crystallite size from 120(3) K (d_{cryst} = 13 nm) to 155(3) K (d_{cryst} = 16 nm), and to 160(3) K (d_{cryst} = 20 nm) after calcining at 350, 500, and 600 °C, respectively. Additionally, T_B decreases with increasing applied field as demonstrated in Fig. S2 (supporting information). The formation of a maximum in the ZFC curve and the increasing of the FC curve at low temperatures indicate a superparamagnetic behaviour of the samples [38,39]. Furthermore, field-dependent magnetization measurements show very small coercivity values at 300 K which considerable increase below the blocking temperature suggesting that most of the particles are in the

superparamagnetic state. Calcining at 800 °C ($d_{cryst.}$ = 83 nm) does not result in any deviation between the FC and ZFC curve and thus no superparamagnetic behaviour. Fig. 8 shows the field-dependent magnetic measurements at 300 K of $Li_{0.5}Fe_{2.5}O_4$ powders depending on calcining temperature and thus on the crystallite size. The saturation magnetization (M_s) was determined by extrapolating of the magnetization at high field to $H^{-1} \rightarrow 0$ [40]. After calcining at 350 °C ($d_{cryst.}$ = 13 nm) the M_s value of 47.0(5) emu g^{-1} is significantly lower than the reported bulk value of about 63 – 65 emu g^{-1} at 300 K [41,42]. The M_s values rise with increasing calcining temperature and thus crystallite size up to 62.2(1) emu g^{-1} after thermal treatment at 1000 °C ($d_{cryst.}$ = 142 nm) (inset in Fig. 8). The reduction of M_s with decreasing crystallite size is due to the increasing in surface-to-volume ratio. At the surface, the collinear spin arrangement found in bulk $Li_{0.5}Fe_{2.5}O_4$ is disturbed because of the incomplete coordination environment of surface ions resulting in a reduced total magnetization [43]. Additionally, higher calcining temperatures lead to an improved crystallinity and thus to a reduction of defects [44,45]. The root-mean-square strain parameter, calculated from the XRD line broadening, reflects the number of crystal lattice defects and decreases from $5(1)\cdot10^{-3}$ to $0.3(1)\cdot10^{-3}$ with increasing calcining temperature to 1000 °C.

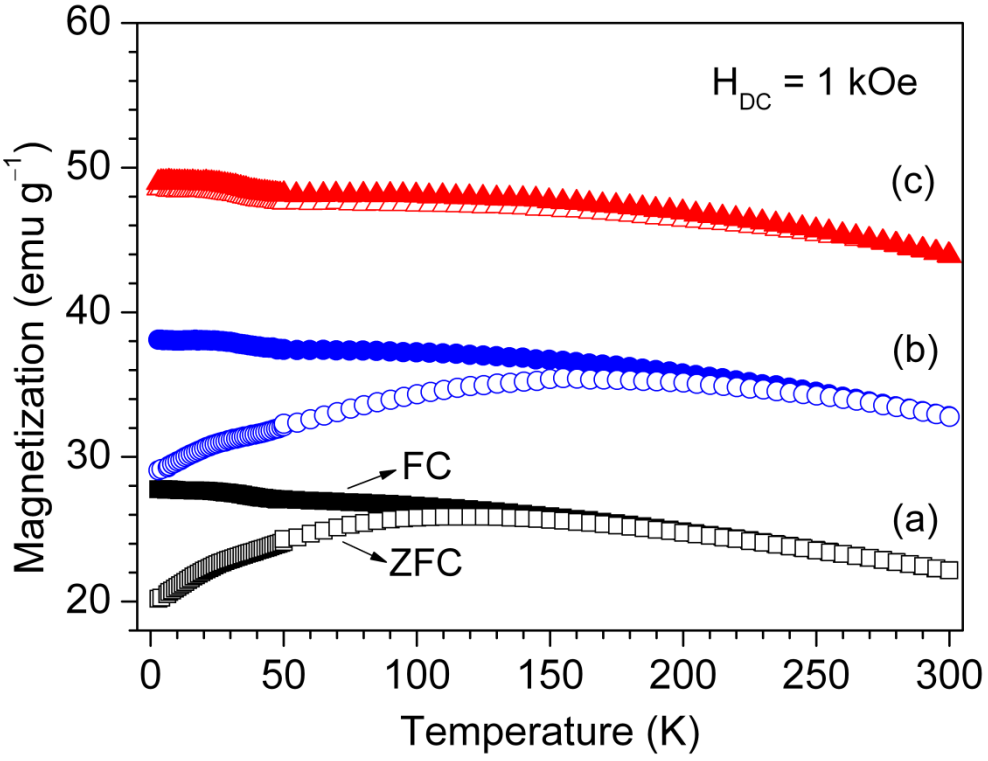

Fig. 7. Temperature dependence of the magnetization under zero-field-cooled (ZFC) and field-cooled (FC) conditions in the range of 3–300 K for powders calcined for 2 h at (a) 350 °C, (b) 600 °C, and (c) 800 °C.

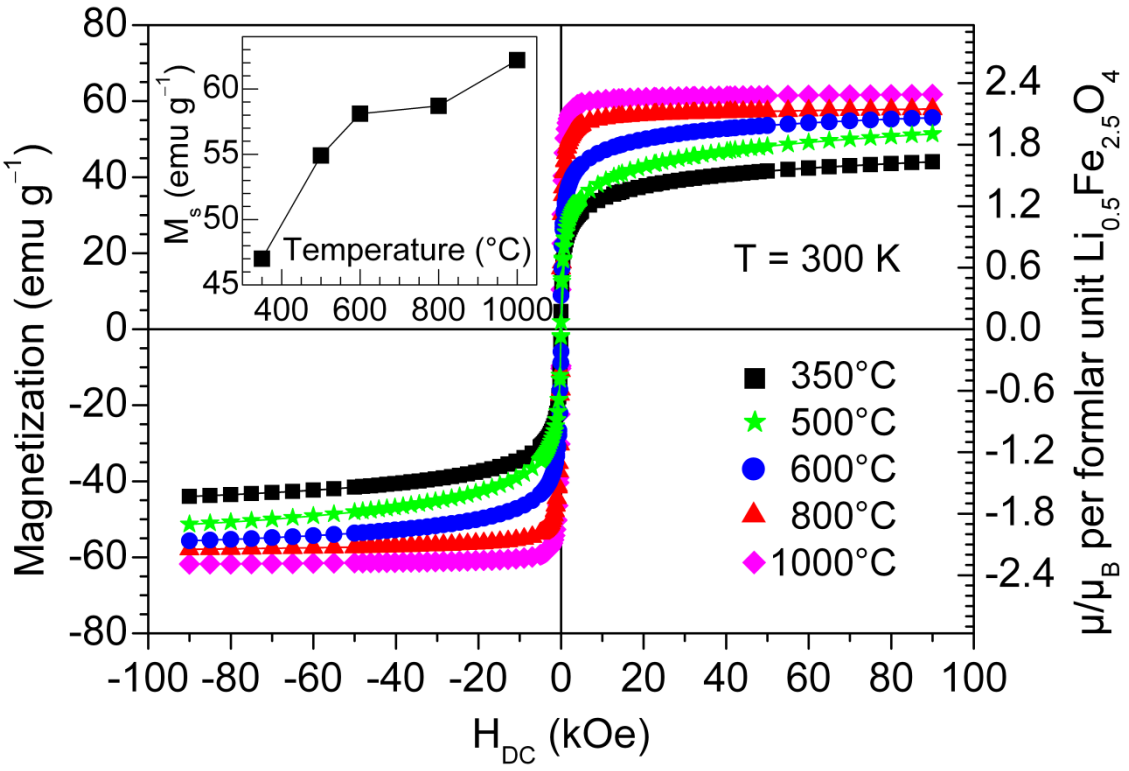

Fig. 8. Magnetization (M) versus applied field (H_{DC}) at 300 K of $Li_{0.5}Fe_{2.5}O_4$ powders calcined at the indicated temperatures for 2 h. The inset shows the saturation magnetization (M_s) at 300 K depending on the calcining temperature. The uncertainties of M_s ($\leq$ 0.5 emu g^{-1}) are smaller than the symbol sizes.

For the sintered ceramic bodies the courses of the magnetization (M) depending on the applied field (H_{DC}) recorded at 3 K are demonstrated in Fig. 9. The ceramics show ferrimagnetic behaviour. The saturation magnetization increases slightly from 70.0(1) to 73.0(1) emu g^{-1} with rising sintering temperature up to 1200 °C (inset in Fig. 9). Increasing M_s values with rising heat treatment were already reported in literature [37,46,47]. Pointon and Saull [15] and Ridgley et al. [37] assumed that an increasing of the saturation magnetization above the value for an ideal invers spinel structure (M_s = 2.5 μ_B f.u.$^{-1}$ = 67.4 emu g^{-1}) is caused by the formation of Fe_3O_4 ($M_s^{(bulk)}$ = 4.1 μ_B f.u.$^{-1}$ [48]) or maghemite

($M_s^{(bulk)}$ = 3.3 μ_B f.u.$^{-1}$ ($Fe_{8/3}O_4$) [49]), due to the loss of lithium and the partial formation of Fe^{2+}. If the increasing magnetizations were caused by the formation of magnetite or maghemite the fractions in the ceramic sintered at 1200 °C should be at least 18 and 29 wt%, respectively [50] according to the M_s values at 3 K. However, the measured weight losses after sintering indicate that the fraction of formed magnetite and maghemite can only be 6 and 12 wt%. Additionally, maghemite is unstable at high temperatures [51] and the presence of any iron oxide phases could not be detected in the ceramic samples as aforementioned. Therefore, the observed rising saturation magnetizations cannot be explained by the formation of magnetite or maghemite. We assume that the cause of the change in M_s lies in differences in the cationic ordering. Lithium ferrite is an inverse spinel and can be written with the general formula $^{T}[Fe_xLi_{0.5-x/2}]^{O}[Fe_{2.5-x}Li_{x/2}]O_4$. The inversion parameter x reflects the Fe^{3+} cations occupying the tetrahedral site with x = 1 for a full invers structure. Considering the measured lithium losses, the M_s values correspond to 2.592(6) – 2.695(6) μ_B f.u.$^{-1}$ ($Li_{0.5}Fe_{2.5}O_4$) after sintering from 1050 to 1200 °C. It can be supposed, that the observed rising M_s values are primarily due to a decrease of the inversion parameter. The loss of lithium during sintering leaves vacancies in the spinel structure which most likely influence the cation distribution between the tetrahedral and octahedral sites. From the M_s values at 3 K, the inversion parameters (x) were calculated as 0.9908(6), 0.9887(6), 0.9864(6), and 0.9805(6) for ceramics sintered at 1050, 1100, 1150, and 1200 °C for 1 h, respectively. Whereas, sintering at 900 °C (weight loss < 0.06 wt%) leads to a M_s value of 67.8(1) emu g^{-1} corresponding to an inversion parameter of 0.9987(6), i.e. very close to the theoretical value of 1. On the other hand, further increasing of the sintering temperature to 1250 °C results in a reduced saturation magnetization of 67.7(1) emu g^{-1} due to the formation of antiferromagnetic Fe_2O_3 (hematite) [52], detected by XRD (see Fig. 6), as a result of the considerable loss of lithium.

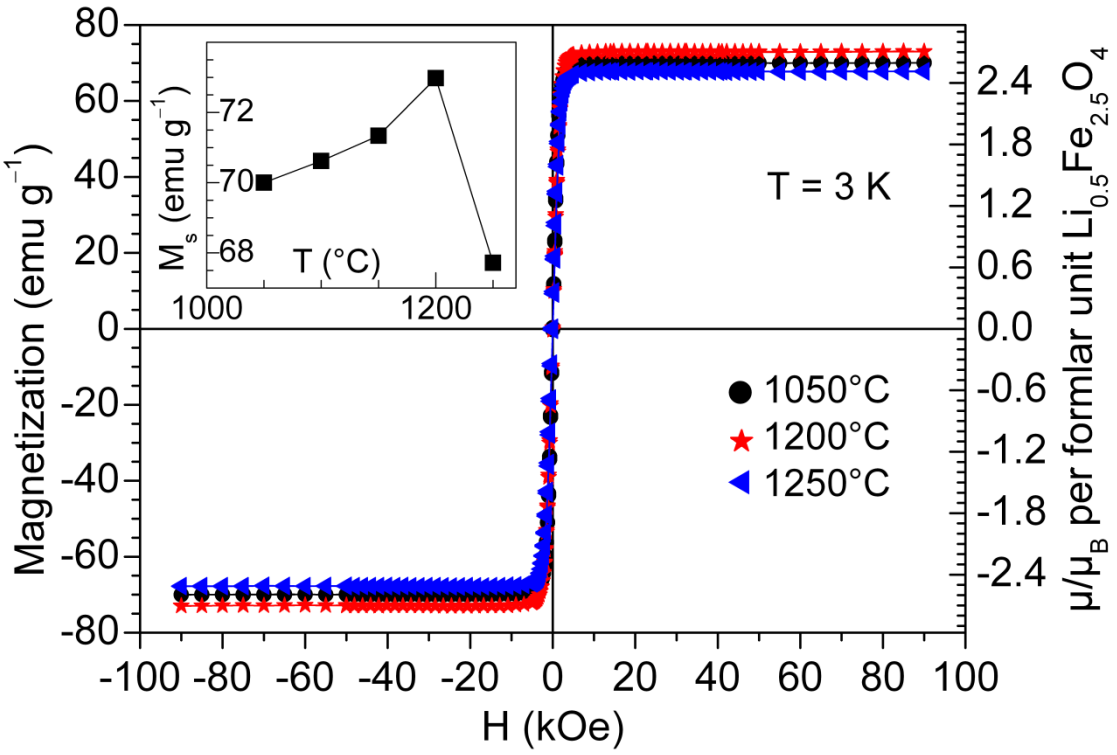

Fig. 9. Magnetization (M) versus applied field (H_{DC}) at 3 K of ceramic bodies sintered at the indicated temperatures for 1 h. The inset shows the saturation magnetizations (M_s) at 3 K depending on the sintering temperature. The uncertainty of M_s (0.1 emu g^{-1}) is smaller than the symbol size.

DSC measurements up to 900 °C reveal both the transition from the ordered to the disordered structure (~ 750 °C) and the ferrimagnetic ⇆ paramagnetic (~ 630 °C) transition (Fig. 10) [53–55]. The ordered ⇆ disordered phase transition temperature (T_{trs}) was determined from the onset of the DSC signal and was found to be T_{trs} = 755(1) °C with $\Delta_{trs}H$ = 13.5(4) J g^{-1} for ceramics sintered between 1050 and 1150 °C. Higher sintering temperatures of 1200 and 1250 °C lead to a slightly reduced transition temperature of 751(1) °C and a decreasing enthalpy of 13.1(4) and 11.8(4) J g^{-1}, respectively. The significant reduction of $\Delta_{trs}H$ after sintering at 1250 °C is primarily caused by the formation of hematite. Reported values for $Li_{0.5}Fe_{2.5}O_4$ are between T_{trs} = 745–768 °C and $\Delta_{trs}H$ = 11–18 J g^{-1} [14,31,56,57]. DSC investigations on $Li_{0.5}Fe_{2.5}O_4$ powders calcined at 350, 500, 600, 800, and 1000 °C ($d_{cryst.}$ = 13–142 nm) show ordered ⇆ disordered transition temperatures of 734(2), 734(2), 739(2), 750(2), and 751(1) °C, respectively. The corresponding enthalpy changes were calculated as 5.0(6), 6.4(6),

8.5(6), 11.9(4), and 12.4(4) J g^{-1} (Fig. 11). The DSC investigations of the ordered ⇆ disordered phase transition show that a reduction of the particle size leads to a significant smaller enthalpy change and to lower transition temperatures mainly due to a surface effect in small particles [58,59]. The thermoanalytical behaviour of $Li_{0.5}Fe_{2.5}O_4$ powders calcined at 800 °C and higher (crystallite size >> 20 nm) are close to the bulk specimens.

The magnetic transition (ferrimagnetic ⇆ paramagnetic) is clearly seen in DSC curves of the sintered ceramics as a weak broad peak (inset in Fig. 10). The Curie temperature (onset temperature) for all sintered ceramics could be estimated as 625(5) °C, whereas the broad magnetic transition peak becomes weaker after sintering at 1250 °C. The nanocrystalline powders calcined at 800 and 1000 °C reveal only a very weak hump between 610 and 640 °C, whereas nano-powders calcined below 800 °C do not show any significant DSC signal because of the very low enthalpy change.

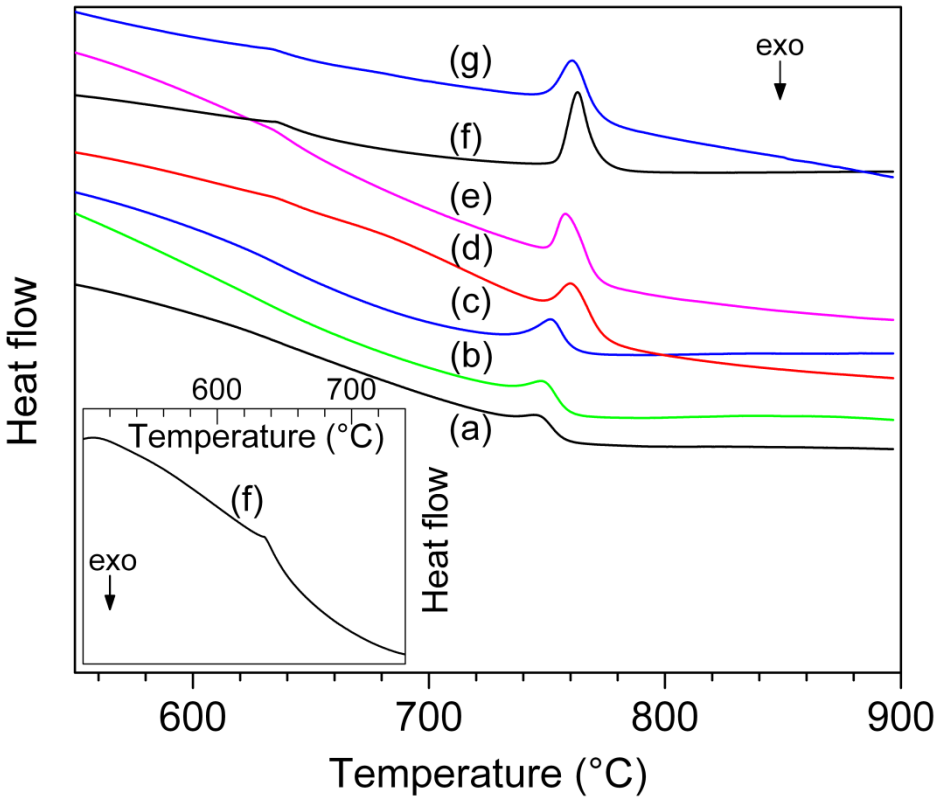

Fig. 10. DSC measurements in flowing air (heating rate 20 K min^{-1}) on powders calcined at (a) 350 °C, (b) 500 °C, (c) 600 °C, (d) 800 °C, (e) 1000 °C and ceramics sintered at (f) 1050 °C, and (g) 1250 °C. The inset shows a magnification of the magnetic transition peak of curve (f).

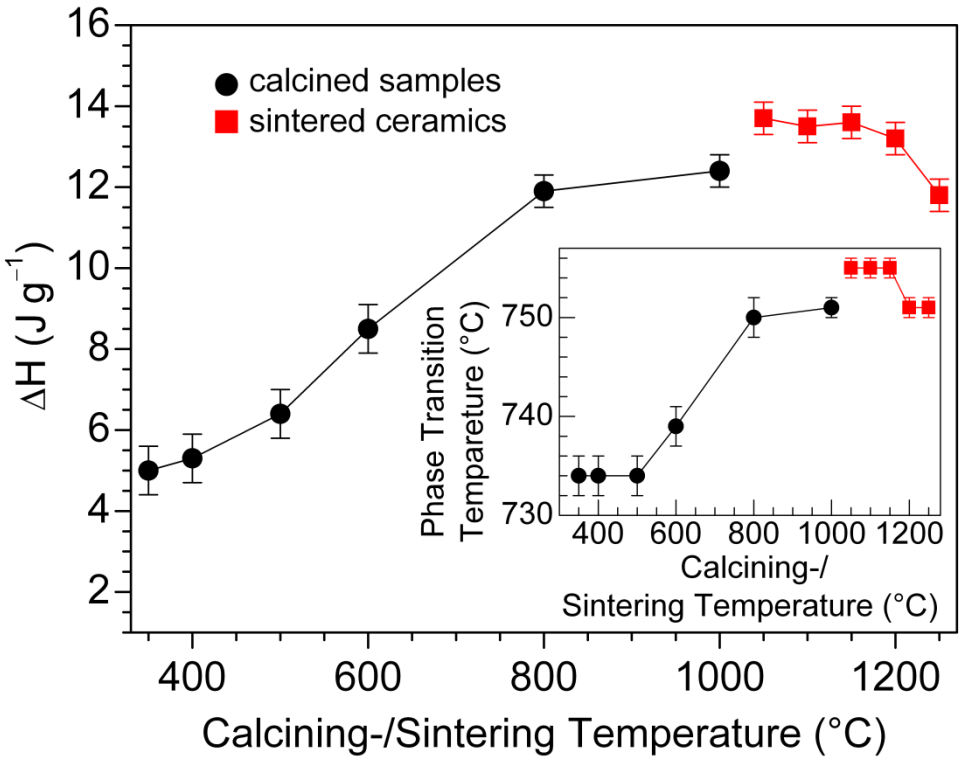

Fig. 11. Dependence of the enthalpy change ($\Delta_{trs}H$) of the order ⇆ disorder phase transition on the thermal treatment. The inset shows the phase transition temperature versus thermal treatment.

Fig. 12 shows the cooling curve of the dilatometric measurement of a ceramic body sintered at 1100 °C. The ordered ⇆ disordered phase-transition caused a sudden length change pointing to a first-order transition. The phase transition temperature of 755(1) °C was determined at the point of inflection. From the dilatometric data, the linear thermal expansion coefficient (α_{dil}) of the bulk ceramic was determined according to Eq. (1) [60]:

$$\alpha_{dil} = \frac{\Delta L}{L_0 \Delta T} \qquad (1)$$

(L_0 – length of the ceramic body at RT, ΔL – length change in the temperature range ΔT). Calculations up to 700 °C (below the phase transition) reveal a linear thermal expansion coefficient of $\alpha_{dil} = 11.4(7) \cdot 10^{-6}$ K^{-1} in good agreement with the value found by Kato [56].

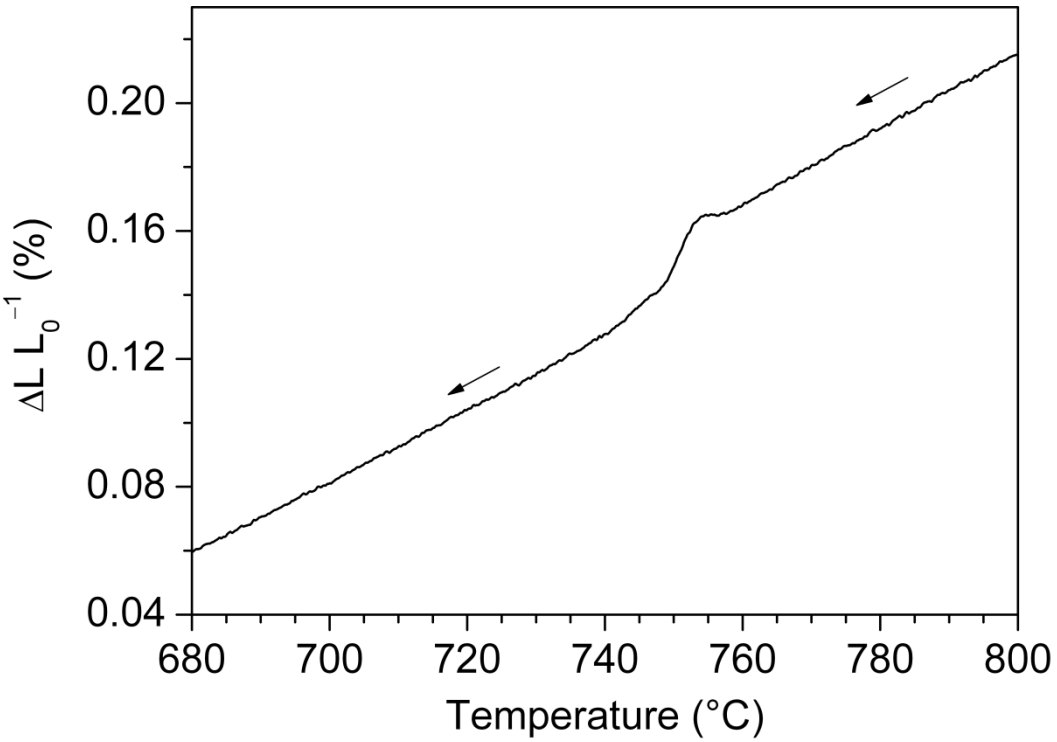

Fig. 12. Dilatometric measurement in flowing air of a ceramic body sintered at 1100 °C during the order ⇆ disorder phase transition (cooling curve, rate 5 K min^{-1}).

Diffuse reflectance spectra of calcined and sintered $Li_{0.5}Fe_{2.5}O_4$ samples were recorded to determine the optical band gap using the *Kubelka–Munk* theory [61,62] in which the optical band gap can be expressed by Eq. 2 [63]:

$$F(R)\cdot h\nu = k(h\nu - E_g)^{1/n} \qquad (2)$$

($F(R)$ – Kubelka–Munk function, k – energy-independent constant, E_g – optical band gap, n – exponent reflecting the type of transition: direct allowed n = 2, indirect allowed n = 1/2 and direct and indirect forbidden transitions n = 2/3 and 1/3). The optical band gap can be obtained by plotting of $(F(R)\cdot h\nu)^n$ versus $h\nu$ and extrapolating the slope to $F(R) \rightarrow 0$ (inset in Fig. 13). Reported optical band gaps for $Li_{0.5}Fe_{2.5}O_4$ are between 1.4 and 2.2 eV assuming direct allowed as well as indirect allowed transition mechanisms [8,9,27,64]. To verify the type of transition, the exponent n can be estimated by linearization of Eq. 2 as described in [62,65]. Briefly, $d(\ln(F(R)\cdot h\nu)/d(h\nu)$ vs. $h\nu$ thus shows a maximum, which can

be used as an approximated value for E_g. The exponent *n* can be obtained as an inverse slop in the plot of $\ln(F(R)\cdot h\nu)$ vs. $\ln(h\nu - E_g)$ (Fig. S3, supporting information). The exponent *n* was found to be ≈ 0.5 (indirect allowed transition) for both the calcined and the sintered samples. For the nano-sized powder calcined at 350 °C, the band gap was calculated as 1.93(2) eV which slightly decreases with increasing crystallite size to 1.81(5) eV at a calcination temperature of 1000 °C. After sintering at 1050 °C the band gap is 1.77(3) eV and decreases to 1.60(3) eV at 1250 °C (Fig. 13). The reduction of the band gap with rising sintering temperature is most likely due to the loss of lithium. Whereas, the higher band gap energy for the nano-sized samples compared to the sintered ones (bulk) is due to the well-known size effect [66,67].

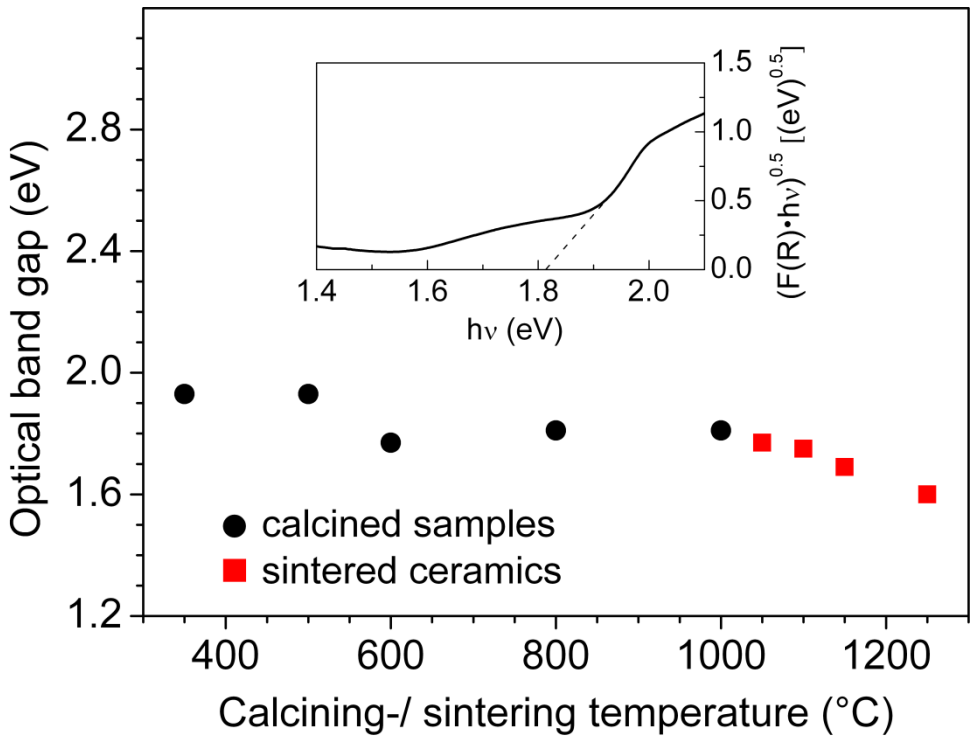

Fig. 13. Indirect-allowed band gap energies for samples calcined between 350 and 1000 °C and ceramics sintered between 1050 and 1250 °C. The inset shows $(F(R)\cdot h\nu)^{0.5}$ versus $h\nu$ for a sample calcined at 1000 °C for 2 h. The uncertainties (≤ 0.05 eV) of the band gap values are smaller than the symbol sizes.

4. Conclusion

Nanocrystalline $Li_{0.5}Fe_{2.5}O_4$ powders were synthesized by a combustion-like soft-chemistry route using starch as gellant agent. Calcining at 350 °C leads to a light-brown powder with a specific surface area of 35(3) $m^2\ g^{-1}$ and a crystallite size of 13(1) nm. The nanocrystalline samples show a superparamagnetic behaviour which vanished above a calcination temperature of 600 °C ($d_{cryst} >> 20$ nm). From the nanocrystalline powder ceramic bodies with variable microstructure are available. After 1 h sintering, dense ceramics (relative density ≥ 90 %) can be obtained at 1100 °C. The calculated optical band gap for $Li_{0.5}Fe_{2.5}O_4$ reveals an indirect allowed transition with values between 1.93(2) and 1.60(3) eV depending on the thermal treatment and particle size. The order ⇆ disorder phase transition for ceramic specimens (bulk) occurs at 755(1) °C with $\Delta_{trs}H$ = 13.5(4) kJ mol^{-1}. While for nanocrystalline powders the transition temperature and the enthalpy change decrease up to 734(2) °C and 5.0(6) kJ mol^{-1} because of an increase of the surface-to-volume ratio. The linear thermal expansion coefficient of bulk $Li_{0.5}Fe_{2.5}O_4$ was determined as $11.4(7)\cdot10^{-6}\ K^{-1}$. Temperature-dependent magnetization curves reveal a superparamagnetic behaviour with blocking temperatures between 120(3) and 160(3) K (H_{DC} = 1 kOe) for nanocrystalline powders with crystallite sizes up to about 20 nm. The ceramic bodies show saturation magnetizations up to 72.99(6) emu g^{-1} at 3 K. M_s increases with rising sintering temperature most likely due to a change of the inversion parameter caused by the formation of vacancies as a result of the rising loss of lithium. The synthesis route described in this article leads to the formation of phase-pure $Li_{0.5}Fe_{2.5}O_4$ at much lower calcining temperature compared to other soft-chemistry syntheses. Due to the large specific surface areas, the nanocrystalline powders are promising candidates for application as catalysts.

Acknowledgements

I am grateful to Prof. Dr. S.G. Ebbinghaus for his helpful discussions. This publication was funded by the German Research Foundation within the Collaborative Research Centre 762 (project A8).

Appendix A. Supplementary data

Supplementary data associated with this article can be found, in the online version, at http://dx.doi.org/

Captions

Fig. 1

Room-temperature XRD patterns of the (LiFe)-gel after calcination for 2 h at different temperatures (heating rate 5 K/min): a) 300 °C, b) 350 °C, c) 500 °C, d) 600 °C, and e) 1000 °C. The insets show a magnification of XRD patterns recorded with a prolonged counting time of 10 s and 40 s per data point, respectively. The reflections marked by an asterisk are superstructure reflections.

Fig. 2

Evolution of the crystallite size with the calcining temperature. The right scale shows the development of the specific surface area.

Fig. 3

Bulk densities of ceramic bodies after sintering at various temperatures (soaking time 1 h, heating rate 5 K min^{-1}). Error bars correspond to the size of the symbols.

Fig. 4

SEM-BSE images of ceramic bodies sintered for 1 h at (a) 1100 °C, (b)1150 °C, (c) 1200 °C, and (d) 1250 °C.

Fig. 5

Thermogravimetric measurement (rate 5 K min^{-1}) of a $Li_{0.5}Fe_{2.5}O_4$ compact in flowing air. The inset shows the total weight loss and the calculated lithium loss after 1 h sintering.

Fig. 6

Room temperature XRD patterns of powdered $Li_{0.5}Fe_{2.5}O_4$ ceramics fired for 1 h at (a) 1050 °C, (b) 1200 °C, and (c) 1250 °C. The patterns were recorded with a counting time of 10 s per data point. The inset shows magnifications of graphs (a) and (c) including the $K\alpha_2$ reflections.

Fig. 7

Temperature dependence of the magnetization under zero-field-cooled (ZFC) and field-cooled (FC) conditions in the range of 3–300 K for powders calcined for 2 h at (a) 350 °C, (b) 600 °C, and (c) 800 °C.

Fig. 8

Magnetization (M) versus applied field (H_{DC}) at 300 K of $Li_{0.5}Fe_{2.5}O_4$ powders calcined at the indicated temperatures for 2 h. The inset shows the saturation magnetization (M_s) at 300 K depending on the calcining temperature. The uncertainties of M_s (≤ 0.5 emu g^{-1}) are smaller than the symbol sizes.

Fig. 9

Magnetization (M) versus applied field (H_{DC}) at 3 K of ceramic bodies sintered at the indicated temperatures for 1 h. The inset shows the saturation magnetizations (M_s) at 3 K depending on the sintering temperature. The uncertainty of M_s (0.1 emu g^{-1}) is smaller than the symbol size.

Fig. 10

DSC measurements in flowing air (heating rate 20 K min^{-1}) on powders calcined at (a) 350 °C, (b) 500 °C, (c) 600 °C, (d) 800 °C, (e) 1000 °C and ceramics sintered at (f) 1050 °C, and (g) 1250 °C. The inset shows a magnification of the magnetic transition peak of curve (f).

Fig. 11

Dependence of the enthalpy change ($\Delta_{trs}H$) of the order ⇆ disorder phase transition on the thermal treatment. The inset shows the phase transition temperature versus thermal treatment.

Fig. 12

Dilatometric measurement in flowing air of a ceramic body sintered at 1100 °C during the order ⇆ disorder phase transition (cooling curve, rate 5 K min^{-1}).

Fig. 13

Indirect-allowed band gap energies for samples calcined between 350 and 1000 °C and ceramics sintered between 1050 and 1250 °C. The inset shows $(F(R)\cdot h\nu)^{0.5}$ versus $h\nu$ for a sample calcined at 1000 °C for 2 h. The uncertainties (≤ 0.05 eV) of the band gap values are smaller than the symbol sizes.

References

[1] K. Hayashi, R. Fujikawa, W. Sakamoto, M. Inoue, T. Yogo, J. Phys. Chem. C 112 (2008) 14255–14261.
[2] G. F. Dionne, Proc. IEEE 63 (1975) 777–789.
[3] V. G. Harris, IEEE Trans. Magn. 48 (2012) 1075–1103.
[4] W. Zhou, Y. Wang, L. Zhang, G. Song, S. Cheng, Int. J. Electrochem. Sci. 10 (2015) 5061–5068.
[5] M. Catti and M. Montero-Campillo, J. Power Sources 196 (2011) 3955–3961.
[6] Y.-M. Dai, Y.-F. Wang, C.-C. Chen, Catal. Comm. 106 (2018) 20–24.
[7] S. B. Gaikwad, B. K. Shelke, S. S. Rokade, S. R. Bembalkar, Int. J. Appl. Res. 2 (2016) 156–158.
[8] D. Zhang and L. Zhang, New. J. Chem. 40 (2016) 7171–7180.
[9] S. Waitz, C. Suchomski, T. Brezesinski, R. Marschall, ChemPhotoChem 2 (2018) 1022–1026.
[10] N. Rezlescu, C. Doroft, E. Rezlescu, P. D. Popa, Sens. Actuators, B 133 (2008) 420–425.
[11] R. Liu, L. Pan, S. Peng, L. Qin, J. Bi, J, Wu, H, Wu, Z.-G. Ye, J. Mater. Chem. C 7 (2019) 1999–2004.
[12] G. R. Gajula, L. R. Buddiga, K. N. Chidambara Kumar, M. Dasari, J. Mater. Sci.: Mater. Electron. 30 (2019) 1262–1274.
[13] A. Thomas and P. Laruelle, Acta Cryst. C 39 (1983) 1615–1617.
[14] A. P. Surzhikov. T. S. Frangulyan, S. A. Ghyngazov, E. N. Lysenko, J. Therm. Anal. Calorim. 108 (2012) 1207–1212.
[15] A. J. Pointon and R. C. Saul, J. Am. Ceram. Soc. 52 (1969) 157–160
[16] G. Bandyopadhyay and R. M. Fulrath, J. Am. Ceram. Soc. 57 (1974) 182–186.
[17] S. A. Mazen and N. I. Abu-Elsaad, Appl. Nanosci. 5 (2015) 105–114.
[18] X. Wang, L. Gao, L. Li, H. Zheng, Z. Zhang, W. Yu, Y. Qian, Nanotechnol. 16 (2005) 2677–2680.
[19] B. Li, H. Su, Y. Qian, X. Liu, Solid State Ionics 120 (1999) 251–254.
[20] A. M. Samy and E. H. Aly, Mater. Sci. Appl. 6 (2015) 436–444.
[21] M. George, S. S. Nair, A. S. M. John, P. A. Joy, M. R. Anantharaman, J. Phys. D: Appl. Phys. 39 (2006) 900–910.
[22] K. Zheleznikov, E. Shalaeva, D. Kellerman, Am. J. Mater. Res. 4 (2017) 15–22.
[23] S. Verma and P. A. Joy, J. Appl. Phys. 98 (2005) 124312.
[24] G. Bonsdorf, H. Langbein, K. Knese, Mater. Res. Bull. 30 (1995) 175–181.
[25] K. U. Kang, S. W. Hyun, C. S. Kim, J. Appl. Phys. 99 (2006) 08M917
[26] M. Dasari, G. R. Gajula, D. H. Rao, A. K. Chintabathini, S. Kurimella, B. Somayajula, Proc. Appl. Ceram. 11 (2017) 7–12.
[27] M. Chireh and M. Naseri, Adv. Powder Technol. 30 (2019) 952–960.
[28] P. Sharma, P. Thakur, J. L. Mattei, P. Queffelec, A. Thakur, J. Magn. Magn. Mater. 407 (2016) 17–23.
[29] M. M. Rashad, M. G. El-Shaarawy, N. M. Shash, M. H. Maklad, F. A. Afifi, J. Magn. Magn. Mater. 374 (2015) 495501.
[30] T. Watari, K. Mishima, T. Torikai, Y. Imaoka, J. Ceram. Soc. Jpn. 106 (1998) 634–636.
[31] N. G. Jovic, A. S. Masadeh, A. S. Kremenovic, B. V. Antic, J. L. Blanus, N. D. Cvjeticanin, G. F. Goya, M. V. Antisari, E. S. Bozin, J. Phys. Chem. C 113 (2009) 20559–20567
[32] T. Zheng, Y. Zhou, W. Ren. H. Cui, Micro Nano Lett. 7 (2012) 991–993.

[33] S. Dey, A. Roy, D. Das, J. Ghose, J. Magn. Magn. Mater. 270 (2004) 224–229.
[34] Program WinXPOW v2.11, Stoe & Cie GmbH, Darmstadt, 2004.
[35] M. I. Mendelson, J. Am. Ceram. Soc. 52 (1969) 443–446.
[36] M. Amemiya, J. Inorg. Nucl. Chem. 34 (1972) 3405–3417.
[37] D. H. Ridgley, H. Lessoff, J. D. Childress, J. Am. Ceram. Soc. 53 (1970) 304–311.
[38] M. Sasaki, P. E. Jönsson, H. Takayama, Phys. Rev. B 71 (2005) 104–405.
[39] T. Bitoh, K. Ohba, M. Takamatsu, T. Shirane, S. Chikazawa, J. Phys. Soc. Jpn. 64 (1995) 1305–1310.
[40] S. Chikazumi, Physics of ferromagnetism. Oxford University Press, Oxford (2005)
[41] G. R. Gajula, L. R. Buddiga, K. N. Chidambara Kumar, Ch. Arun Kumar, M. Dasari, J. Sci: Adv. Mater. Devices 3 (2018) 230–235
[42] G. O. White and C. E. Patton, J. Magn. Magn. Mater. 9 (1978) 299–317.
[43] R. H. Kodama, J. Magn. Magn. Mater. 200 (1999) 359–372.
[44] S. Singh, S. Munjal, N. Khare, J. Magn. Magn. Mater. 386 (2015) 69–73.
[45] Z. Nedelkoski, D. Kepaptsoglou, L. Lari, T. Wen, R. A. Booth, S. D. Oberdick, P. L. Galindo, Q. M. Ramasse, R. F. L. Evans, S. Majetich, V. K. Lazarov, Sci. Rep. 7 (2017) 45997.
[46] V. Verna, V. Pamdey, S. Singh, R. P. Aloysius, S, Annapoorni, R. K. Kotanala, Physica B 404 (2009) 2309–2314.
[47] S. S. Teixeira, M. P. F. Graça, L. C. Costa, M. A. Valente, Mater. Sci. Eng. B 186 (2014) 83–88.
[48] R. Pauthenet and L. Bochirol, J. Phys. Radium 12 (1951) 249–251.
[49] C. J. Goss, Phys. Chem. Minerals 16 (1988) 164–171.
[50] T. J. Daou, J. M. Grene`che, G. Pourroy, S. Buathong, A. Derory, C. Ulhaq-Bouillet, B. Donnio, D. Guillon, S. Begin-Colin, Chem. Mater. 20 (2008) 5869–5875.
[51] S. Grimm, T. Stelzner, J. Leuthäußer, S. Barth, K. Heide, Thermochim. Acta. 300 (1997) 141–148.
[52] P. J. Flanders and J. P. Remeika, Philos. Mag. 11 (1965) 1271–1288.
[53] M. Vucinic-Vasic, B. Antic, J. Blanusa, S. Rakic, A. Kremenović, A. S. Nikolic, A. Kapor, Appl. Phys. A 85 (2006) 49–54.
[54] S. A. Mazen and T. E. Whall, J. Magn. Magn. Mater. 43 (1984) 221–226.
[55] J. Darul, W. Nowicki, P. Piszora, C. Baehtz, E. Wolska, J. Alloys Compd. 401 (2005) 60–63.
[56] E. Kato, Bull. Chem. Soc. Jpn. 31 (1958) 113–117.
[57] V. Berbenni, A. Marini, D. Capsoni, Z. Naturforsch. 53a (1998) 997–1003.
[58] R. Köferstein, L. Jäger, M. Zenkner, S.G. Ebbinghaus, Mater. Chem. Phys. 119 (2010) 118–122.
[59] R. Lipowsky, Ferroelectrics 73 (1987) 69–81.
[60] J. D. James, J. A. Spittle, S. G. R. Brown, R. W. Evans, Meas. Sci. Technol. 12 (2001) R1–R15.
[61] P. Kubelka and F. Munk, Z. Techn. Phys. 11 (1931) 593–601.
[62] R. Köferstein and S. G. Ebbinghaus, J. Eur. Ceram. Soc. 39 (2019) 1156–1163.
[63] O. Schevciw and W. B. White, Mater. Res. Bull. 18 (1983) 1059–1068.
[64] R. R. Chilwar, A. R. Chavan, M. K. Babrekar, K. M. Jadhav, Physica B 566 (2019) 43–49.
[65] J. Tang, Z. Zou, J. Ye, J. Phys. Chem. B 107 (2003) 14265–14269.
[66] S. N. Sahu and K. K. Nanda, PINSA A 67 (2001) 103–130.
[67] E. Roduner, Chem. Soc. Rev. 35 (2006) 583–592.